Evolution and breakdown of helical vortex wakes behind a wind turbine

A. Nemes[1], M. Sherry, D. Lo Jacono[1,2,3], H. M. Blackburn[4] and J. Sheridan[1]

[1] Fluids Laboratory for Aeronautical and Industrial Research (FLAIR), Department of Mechanical and Aerospace Engineering, Monash University, Melbourne, Vic 3800, Australia
[2] Université de Toulouse; INPT, UPS; IMFT; Allée Camille Soula, F-31400 Toulouse, France
[3] CNRS; IMFT; F-31400 Toulouse, France
[4] Department of Mechanical and Aerospace Engineering, Monash University, Melbourne, Vic 3800, Australia

E-mail: andras.nemes@monash.edu

Abstract. The wake behind a three-bladed Glauert model rotor in a water channel was investigated. Planar particle image velocimetry was used to measure the velocity fields on the wake centre-line, with snapshots phase-locked to blade position of the rotor. Phase-locked averages of the velocity and vorticity fields are shown, with tip vortex interaction and entanglement of the helical filaments elucidated. Proper orthogonal decomposition and topology-based vortex identification are used to filter the PIV images for coherent structures and locate vortex cores. Application of these methods to the instantaneous data reveals unsteady behaviour of the helical filaments that is statistically quantifiable.

1. Introduction

The blades of rotor systems – whether wind turbines, propellers, or helicopter rotors – shed vortices into the wake that advect downstream and are described by helical paths. The evolution and breakdown dynamics of these vortical wakes is not fully understood and remains an important question in wind energy [1], aviation [2, 3], and marine industries [4]. It is also of fundamental interest in the field of vortex dynamics [5, 6, 7].

The dominant vortical structures in the wake of horizontal axis wind turbines (HAWTs) are counter rotating helical vortex pairs, comprising of a tip and root vortex shed from each blade of the turbine. These vortices play an important role in the evolution of the wake directly downstream of the turbine, known as the near-wake, and hence on the resultant wake far downstream of the turbine, the far wake. Naturally, the wakes of turbines operating at full scale are strongly influenced by the atmospheric boundary layer (ABL). The ABL introduces shear and large turbulent scales that interact with the turbine wake causing large scale wake motion [8] and asymmetric wake evolution [**?**]. A comprehensive review of the many variables influencing full-scale turbine wakes is provided in [9]. From a wind energy perspective, coherent tip and root vortex structures in the near-wake may affect turbine performance and generate noise [10], whereas the breakdown dynamics of these helical vortex structures influence the characteristics of the resultant wake far downstream. This has direct consequences in wind farms where the

interaction between a turbine and the wake of an upstream turbine may introduce dynamic loading on blades and lead to a drop in wind farm performance [11].

Such challenges in industry have seen a renewed interest in the fundamental problem of the evolution and breakdown of helical vortices. Early stability analysis [6] highlighted three general instability modes when a single helical filament is perturbed; short-wave and long-wave modes along the vortical filament, and a mutual induction mode where subsequent turns of the helix interact. Analysis of rotor wake models has led to more complex analytical configurations of multiple tip vortex filaments, which have been investigated with [1, 7] and without [5] a hub vortex. The hub vortex is typically modelled as a single axial vortex of opposite sign and strength to the sum of the tip vortices, as prescribed by the Joukowsky wake. In all these analytical investigations the stability of inviscid models of helical systems with the root vortex have been found to be inherently unstable. Nevertheless, experimental observations [4, 14], and numerical results [15] report the tip vortices persisting for a significant distance downstream. It has been proposed [1] that analytical modelling of the stability of rotor wakes requires a relaxation of the ideal constant circulation blade assumption and inclusion of the blade wake due to the important role the blade wake plays in the vortex interactions of the system. The stability analysis [1] of helical vortices embedded in assigned flow fields showed that the stability conditions are strongly dependent on the radial distribution of the assigned vorticity fields, supporting the hypothesis that the tip and hub vortex interaction stabilises an otherwise inherently unstable system.

Experimental flow visualisations [16] and numerical simulations [17] have all shown that the tip vortices behind rotors undergo mutual inductance, with a resulting entanglement and coalescence of vortices [3, 4]. This is a result of the Biot-Savart law, and corresponds to the mutual inductance mode in linear stability studies [6]. However, recent flow visualisations [4] revealed the filament pairing of a three-bladed rotor is initiated by different physics to that proposed by numerical simulations shown in [17]. The former showed the filament pairing as a multi-step process whereby two filaments interact first and then interact with the third, while in the latter all three filaments interact simultaneously. The experiment studied the wake of marine propellers, not turbines, and although the wake symmetry is analogous [10], the two systems are not completely similar.

Recent full scale PIV measurements [18] have provided an invaluable first quantitative view of the characteristics of full-scale tip vortices. Such studies are desirable but costly. They also suffer from having a limited spatial dynamic range imposed by PIV configurations, which restrict their capacity to fully study the evolution and characteristics of the vortical structures. As such, small-scale water channel experiments are essential to allow characterisation of the interaction between the vortices, as they provide sufficient resolution to resolve the induced velocities of the multiple vortices. The current paper investigates the wake of a three-bladed model HAWT. As the wake of a wind turbine is a multiple vortex system, phase-locked field measurements are required to investigate the vortices at a particular blade phase angle. First, a description of the experimental rotor and method is given. The post-processing techniques are then described, followed by results and discussion of the phase-locked measurements of the turbine wake.

2. Experimental method

2.1. Glauert optimum rotor

A drawback of small-scale experimental models is the reduced performance of the rotor airfoils. Pure geometric scaling leads to poor dynamic scaling and as a result the wake becomes unsuitable for studying instabilities [19]. A rotor design based on the [20] optimum rotor was used to maximise power output, and hence maximised bound circulation along the blade. The three-bladed optimum Glauert rotor used in the experiments was designed for an operational tip speed ratio, $\lambda_d = \Omega R/\boldsymbol{U}_\infty = 3.5$, where $\boldsymbol{U}_\infty$ is the freestream velocity, Ω is the rotation rate, and R is the rotor radius. The design λ_d is lower than full scale turbines, $\lambda_f \approx 7$, as the aerodynamic

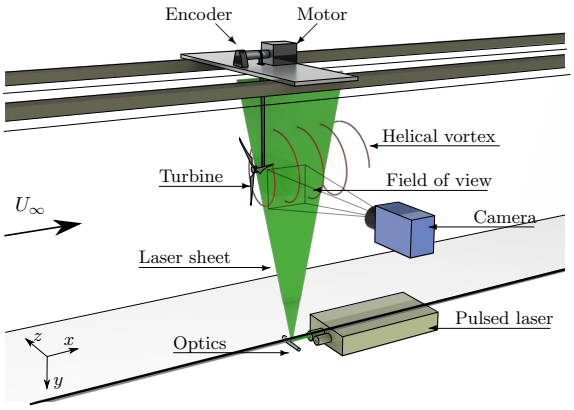

Figure 1. Schematic of the experimental rig. Freestream is from left to right, and the helical path of a single tip vortex is shown as it intersects the measurement plane illuminated by the laser.

performance of the airfoil cross-section, here the NACA4412, is reduced at the investigation Reynolds number which is close to $Re \approx 1.1 \times 10^4$ along the entire span. The blades were optimised using the blade element momentum (BEM) method with the rotor and tip correction formulae of [21] applied. The rotor blades have a radius of $R = 115$mm, and contain both twist and taper to minimise the spanwise variation of blade circulation, $\Gamma_b(r) = c(r)U_{rel}(r)C_L(r)$, where $c(r)$, $U_{rel}(r)$ and $C_L(r)$ are the local blade chord, relative velocity and sectional lift coefficient respectively. By minimising the bound circulation variation, the shed vorticity was focused at the tip and root sections in order to concentrate the tip and root vortices. The lifting surface terminates outside the influence of the nacelle boundary layer to minimise effects of turbine support geometries on root vortex formation [19].

2.2. Experimental setup

The experiments were conducted in the free-surface recirculating water channel of FLAIR in the Department of Mechanical and Aerospace Engineering at Monash University. The water channel facility has a test section of 4000 mm in length, 600 mm in width, and 800 mm in depth. The freestream velocity was $\boldsymbol{U}_\infty = 200\,\mathrm{mms}^{-1}$ and the water temperature monitored during acquisition and varied by less than $\Delta T = 0.1^\circ$ C. The turbine rotor axis was aligned with the channel centre at a depth of 400 mm to avoid interaction with the walls and free-surface.

Particle image velocimetry (PIV) was used to reconstruct 2D velocity fields behind the turbine. The flow was seeded with hollow micropheres (Sphericel 110P8, Potters Industries Inc.) with a nominal diameter of 13 μm and a specific weight of $1.1\,\mathrm{gcm}^{-3}$.

Two Nd:YAG pulsed lasers (Minilite II Q-Switched lasers, Continuum) were directed through optics to produce two 2 mm thick planar sheets pulsed at an interval of Δt apart, illuminating the particles in a vertical-streamwise plane on the wake centre-line. A CCD camera (pco.4000, PCO AG) with double shutter 4008×2672 pixel resolution and equipped with a 105 mm lens (AF105 Nikkor, Nikon Corporation) captured the image pairs of the illuminated plane. In-house cross-correlation software [22] calculated the instantaneous velocity field, ($\boldsymbol{u}_x$, $\boldsymbol{u}_y$), from the image pairs using 32×32 pixel interrogation windows with 50% overlap to give a vector spacing resolution of $8.2 \times 10^{-3}R$. These fields were used to calculate the out-of-plane vorticity ($\boldsymbol{\omega_z}$) vector fields. The experimental setup is shown in figure 1.

The turbine was driven at the required λ by a micro-stepping drive (OEM350–650 and 6K2 Controller, Parker). The drive shaft of the motor was situated above the water channel and a

timing belt transferred the torque to the model turbine shaft through the tower support. An optical encoder (HBM5–1250, US Digital) attached to the drive shaft was used to monitor the turbine speed and blade position.

Measurements were taken of the centre plane of the turbine wake with a field of view (FOV) restricted to the half of the wake that did not include the support geometry. A three-axis traverse (IMC–S8 controller, ISEL) was used to position the camera at multiple downstream locations to capture the wake spatial evolution and maintain a high spatial vector resolution. A total of 800 PIV snapshots were recorded at each camera location up to a streamwise distance $x/R = 5$ downstream. A second set of measurements were take with regions of interest (ROI) centred on tip vortex signature locations, with 700 images per vortex.

2.3. Proper orthogonal decomposition

POD is a flexible mathematical tool to decompose a data-set into a finite sum of weighted orthogonal basis functions. It allows reduced-order modelling of complicated multi-degree-of-freedom dynamic systems, such as fluid flows [23]. The snapshot method of POD allows for low-cost calculation of these basis functions from multiple time instances of measured states. The shape of these basis functions, or modes, may be used to identify correlations across the measured states (mode shapes spanning the state dimensions) or to reconstruct the dynamics of the flow with low-order modelling.

When considering experimental PIV data the measured states are the velocity vector fields of size $nx \times ny$, a given field measured at a given instant in time. The vector fields, each represented as a column vector, are arranged in a matrix, $\boldsymbol{A}$, containing M rows in N columns representing each snapshot in time. For planar PIV the rows are equal to $M = 2(nx \cdot ny)$. The normalised auto-correlation of the observed snapshots is calculated,

$$\boldsymbol{C} = \frac{1}{N}(\boldsymbol{A}, \boldsymbol{A}) \tag{1}$$

where the inner product is defined as $(f, g) = \int f(x) \cdot g(x)dx$. A singular value decomposition (SVD) of $\boldsymbol{C}$ generates N temporal, $\boldsymbol{t}_i$, and state modes, $\boldsymbol{v}_i$, and their singular values, λ_i. The temporal modes are discarded for temporally uncorrelated snapshots. The benefit of the above method (as compared to an eigenvalue decomposition or a direct SVD of $\boldsymbol{A}$) is that the SVD of $\boldsymbol{C}$ provides the singular values ranked by magnitude, and whose units are equal to those of the input matrix, $\boldsymbol{C}$. For the auto-correlation matrix of velocity data the units are $\boldsymbol{u}^2$, and hence related to the kinetic energy of the flow. These inherent properties of the technique aid the physical interpretation of the basis function shapes when analysing fluid flows. The relationship of each mode's energy content and shape to the dynamics of the flow is dependent on the flow in question. The related spatial modes, $\boldsymbol{\Phi}^{(i)}$, are the projections of the state modes, $\boldsymbol{v}_i$ of the decomposition onto the measured states, $A^{(i)}$. The spatial modes then allow the reconstruction of the measured states at a time instant,

$$\boldsymbol{U}^{(i)} = \sum_{j=1}^{N} a_{ij}\boldsymbol{\Phi}^{(j)}, \tag{2}$$

where the coefficients, a_{ij}, are found by projecting the measured velocity onto the orthogonal basis,

$$a_{i,j} = (\boldsymbol{A}^{(i)}, \boldsymbol{\Phi}^{(j)}). \tag{3}$$

2.4. Vortex identification and analysis

This section describes the challenges and approaches in vortex identification and summarises the method introduced by [25] for the identification of vortices in a turbulent flow. Analysis of vortices in wake flows requires robust and accurate methods of vortex identification. The out-of-plane vorticity field, $\boldsymbol{\omega_z}$, calculates the vorticity at a point location. The vorticity field in experimental PIV data is directly available from the measured velocity field, however, it is prone to large variation due to small-scale fluctuations in the velocity field and random error introduced by the PIV technique [26]. Conditional averaging of velocity fields can be used to filter out undesirable unsteady fluctuations and introduced noise while retaining phase information of larger structures. POD and other decomposition techniques may also be used to reconstruct phase information [23] in order to elucidate periodic behaviour. If available, averaging of phase-locked measurements of a flow provide the most robust way of filtering time dependent behaviour, referred to hereafter as phase-averaging. Vorticity fields of phase-averaged data are filtered of the large gradients associated with small-scale fluctuations in the velocity field and allow for reconstruction of the vortex dynamics of such flows. The helical vortices embedded in rotor wakes, however, are highly sensitive to perturbations [6]. The rise of instability modes and mutual inductance of filaments results in time-dependent behaviour of these large-scale structures observed from period to period as a 'meander' of the vortex[**?**]. This vortex meander is obfuscated by phase-averaging which will result in spatial smoothing of the vorticity field. Any characterisation of the helical vortex properties, including vortex strength and core size must therefore account for this vortex meander, requiring analysis of the vortex in instantaneous snapshots.

Vortex identification in a flow-field is a non-trivial process, due in part to the lack of universal analytical definition of a vortex [27]. Many tools for identifying and subsequently quantifying a vortex have been developed, with the popular methods thoroughly reviewed in [27]. The method used in this investigation was introduced by [25] and exploits the flow topology in order to identify large scale vortical structures in a turbulent flow.

The method calculates a scalar field, $\Gamma_1(x, y)$, based on the PIV velocity vector field. The scalar function calculates the velocity field's relative rotation about each grid point constrained to a definable interrogation window. The choice of interrogation window size is dependent on the length-scales of the vortices and background flow length-scales. The discrete scalar function is defined as

$$\Gamma_1(c) = \frac{1}{S} \sum_m \frac{(\boldsymbol{cm} \times \boldsymbol{u}_m) \cdot z}{||\boldsymbol{cm}|| \cdot ||\boldsymbol{u}_m||} \tag{4}$$

where S is the number of grid points, m, within a bounded square region centred on grid point c. The field is equivalent to the calculated ensemble average of $\sin(\theta_m)$ about c, where θ_m is the angle between the radius vector, $\boldsymbol{cm}$ (from the centre of the interrogation window c, to grid point m) and the velocity vector, $\boldsymbol{u}_m$ located at grid point m. This value will approach one of the bounds, $\Gamma_1 = \pm 1$, when calculated at the core of an axi-symmetric vortex. As the function is not Galilean invariant, the instantaneous Lagrangian flow field surrounding each vortex was estimated by subtracting the phase-average velocity from each snapshot. The centres of the vortex cores are identified by the largest absolute peak of the Γ_1 field and sub-grid accuracy was determined by calculating the barycentre of the Γ_1 field.

3. Results

3.1. Phase-averaged wake

Figure 2 shows the normalised phase-averaged streamwise velocity, $\boldsymbol{u}_x/\boldsymbol{U}_\infty$, of the wake behind a turbine operating at $\lambda_d = 3.5$. The measurement plane is aligned with the turbine axis, and the FOV captures the the wake from the rotor plane to an axial distance of $x/R = 5$ downstream. The freestream flow is from left to right. A blade intersects the measurement plane at the chosen

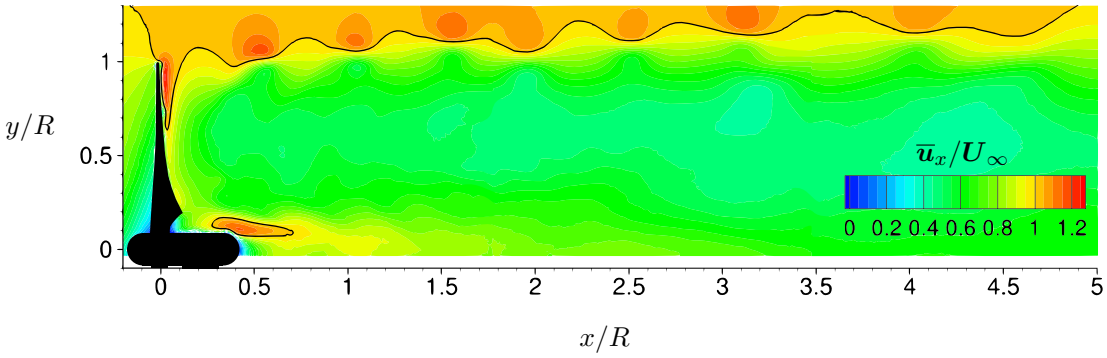

Figure 2. Phase-averaged normalised streamwise velocity contours of the rotor wake for $\lambda_d = 3.5$. Freestream, $\boldsymbol{U}_\infty$, is from left to right. The velocity deficit and wake expansion behind the turbine is evident. The velocity gradients reveal the shear layer at the wake edge. The solid line defines the freestream velocity, $\overline{\boldsymbol{u}}_x = \boldsymbol{U}_\infty$.

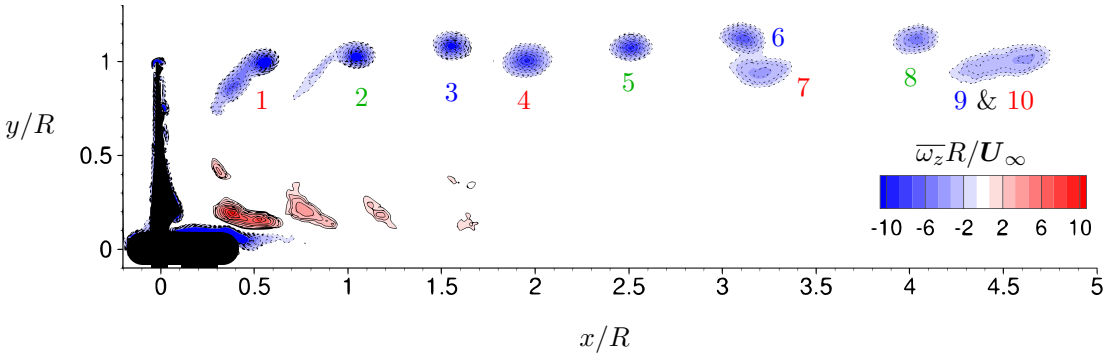

Figure 3. Phase-locked averaged normalised vorticity contours of the rotor wake for $\lambda_d = 3.5$. Dashed isolines (filled blue) represent clockwise (CW) negative vorticity, solid isolines (filled red) represent counter-clockwise (CCW) positive vorticity. Tip vortices (numbered sequentially) are visible in the wake and the roll-up and pairing of vortices is evident.

phase-angle with the tangential velocity vector pointing into the page. The velocity gradients highlight the wake velocity deficit and wake expansion, confirming the rotor is operating in a turbine state. The distribution of the velocity deficit is near constant radially along the blade between $0.2 < y/R < 1$, highlighting good turbine performance. A speed up is evident in the wake near the nacelle trailing edge. This velocity speed-up is generated by the root vortex and nacelle boundary layer interaction, and the trailing edge of the nacelle.

The phase-average shear layer at the wake boundary can be observed in figure 2. The velocity gradients in the shear layer signify the presence of coherent structures in the wake, the tip and root vortices. A slight expansion in the wake is evident, and within the FOV of the measurements no wake recovery is observable.

The turbine's near-wake phase-averaged out-of-plane vorticity field, $\overline{\omega_z}$, non-dimensionalised by $\boldsymbol{U}_\infty$ and R, is shown in figure 3. The tip and root vortices are clearly evident. The vortex cores appear elliptical due to the non-perpendicular intersection angle of the helical filaments with the measurement plane. Adjacent vortices are spaced $V_A = 120°$ apart due to the symmetry of the three bladed turbine, where V_A is the vortex age defined as the azimuthal travel of the blade since filament creation in degrees (°). The tip vortices are numbered sequentially, $n = V_A/120°$.

A pairing phenomenon of the tip vortex helical filaments is captured, with vortex interaction

causing a change in the helical pitch early in the near wake, at $x/R > 1.5$, signifying a breaking of the helical symmetry. The entanglement of the two filaments is evident at $x/R \geq 3$. The evolution of the pairing occurs with the first filament ($n = 3$) displaced radially outward relative to the other ($n = 4$) due to their mutual induction. As the two interacting tip vortices advect further into the wake the filament core at $n = 6$ is accelerated downstream of the other, aged $n = 7$. These two filaments entangle further such that they appear as a single elongated patch of vorticity at $x/R \sim 4.5$ due to the phase-averaging of the vector fields. The symmetry breakdown of the vortex system leads to highly unsteady behaviour and results in spatial averaging of the out-of-plane vorticity field and the phase-averaged tip vortex signature decreases rapidly thereafter. This pairing phenomenon has been seen experimentally in 2-bladed turbine visualisations [16]. The current study confirms the three-bladed interaction, agreeing with prior visualisation of the wake behind a 3-bladed marine propeller [4]. Their propeller configuration differs in that it added energy to the flow and produced a single longitudinal hub vortex as opposed to 3 root vortices. The process here confirms that two of the three filaments experience a pairing, followed by coalescence. The third filament eventually is also entangled and the three intertwined filaments undergo a complex vortex breakdown [4].

Blade wakes are visible at early vortex ages ($n = 1, 2$) in figure 3. These arise from spanwise blade bound circulation gradients ($d\Gamma_b/dr$) and the vorticity sheet of the shear layer formed at blade trailing edge. Figure 3 shows that the tip vortices entrain vorticity from the blade wakes with the roll-up of the trailing vorticity sheet completed by $V_A \leq 360°$. As the blade wakes are entrained into the helical vortex structures interaction with neighbouring vortices upstream is likely.

The root vortex forms near the blade termination point and is advected downstream at a radial position of $y/R = 0.2$. The vortex signatures in the wake decrease rapidly due to their close proximity to the nacelle boundary layer which contains vorticity of opposite sign. Interaction between the two causes vortex cross-annihilation that leads to the decrease in root vortex signatures.

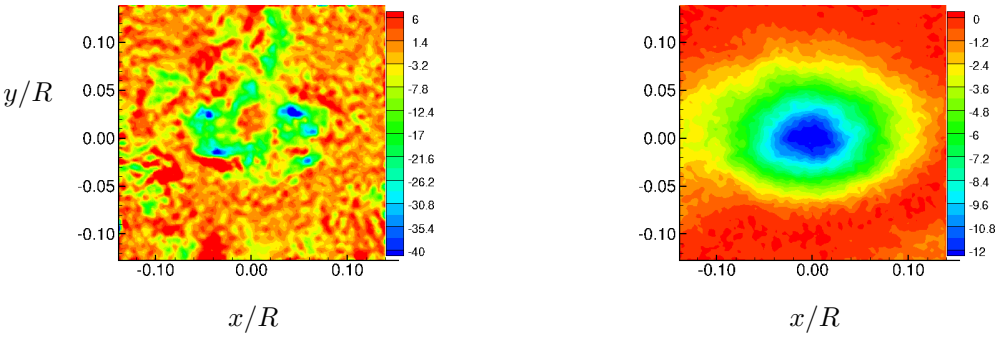

Figure 4. Instantaneous (left) and phase-averaged (right) normalised vorticity contours of tip vortex located $V_A = 240°$ (Tip vortex 2). Note that the contour levels differ between the snapshots due to the large variation in vorticity in the instantaneous snapshots.

3.2. Vortex identification in the wake

An examination of the unsteady behaviour of the helical vortices in the wake was performed using the methods outlined in section 2.3 and 2.4. These methods were applied to instantaneous snapshots at the same phase with an ROI focusing on each tip vortex identified from the phase-averaged vorticity field shown in figure 3. For the purpose of discussing unsteadiness of the flow, the phase average is defined as the mean of the acquired measurements at a given phase. The

vorticity fields of the mean and an instantaneous snapshot of the second tip vortex ($V_A = 240°$) are shown in figure 4.

For each tip vortex the POD of the acquired snapshots resulted in 700 spatial modes. The singular values, λ_i, of the POD of the tip vortex $V_A = 240°$ are plotted in figure 5 for the first 60 modes. The energy contribution of the remaining modes continues to decreases with an exponential trend up to $N = 700$.

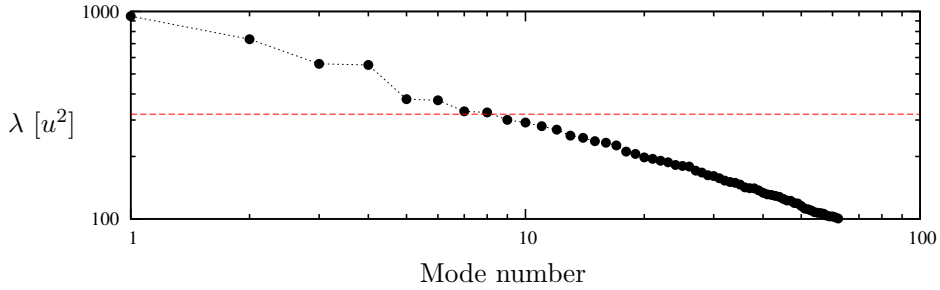

Figure 5. Energy contribution of the first 60 orthogonal modes from the POD of 700 snapshots from tip vortex $V_A = 240°$. The red dashed line represents the mode cut-off used for the reconstruction of the instantaneous thresholds, applying the PIV error criterion of [28].

For the purpose of the method outlined the zero order mode of POD has been retained, which simply equates to the mean of the snapshots. The first 4 velocity mode shapes are shown in figure 6 along with the mean mode (Mode 0) and the vorticity field of the reconstructed snapshot truncated at the 7^{th} mode. Low-order reconstruction of the instantaneous fields requires a truncation criteria for the linear combination of modes. For the purpose of filtering PIV introduced noise, the error threshold of [28] was applied. This threshold requires the singular value of a mode to be above the PIV error threshold, defined by,

$$\lambda_i > \epsilon\sqrt{nx \cdot ny \cdot N} \tag{5}$$

where ϵ is the root mean square error of the PIV technique. The error parameter was chosen as $\epsilon = 0.1\,\text{pixel}/\Delta\text{t}$ following [26]. Modes containing a lower energy contribution are considered to be strongly affected by random artifacts introduced by the PIV technique [28]. The reconstruction of all tip vortices was truncated to the first 7 modes.

The Γ_1 scalar was calculated on all reconstructed instantaneous velocity fields for the first 5 tip vortex signatures. The centroid of the Γ_1 fields provided the instantaneous vortex core locations, allowing a characterisation of the vortex meander. Figure 7 shows a scatter plot of the 700 core locations of tip vortex 2 relative to the mean position.

The results show that the meander of the vortex core are larger in the axial direction in the near-wake. The spread of the core locations can be reasonably well described in both directions by a Gaussian distribution (with a negligible skew), allowing characterisation of the meander of the vortex cores by their standard deviation, σ. The standard deviation was calculated for each tip vortex shown in figure 3 for $V_A \leq 600°$. These results are shown in figure 8.

Three observations can be immediately made: 1) The axial vortex meander is greater than radial meander for all tip vortex locations, 2) the radial meander is consistent for the first four vortices, 3) there is a significant jump in both axial and radial meander at tip 5. The first tip vortex ($V_A = 120°$) has the least meander, an expected result given the vortex filament has just been shed by the blade. The next filament's tip vortex at $V_A = 240°$, shed from the preceding blade, has an increase in axial meander that along with the radial meander remains consistent up until the fourth tip vortex. The jump at $V_A = 600°$ can be expected to be due to breakdown as the other two filaments begin entanglement.

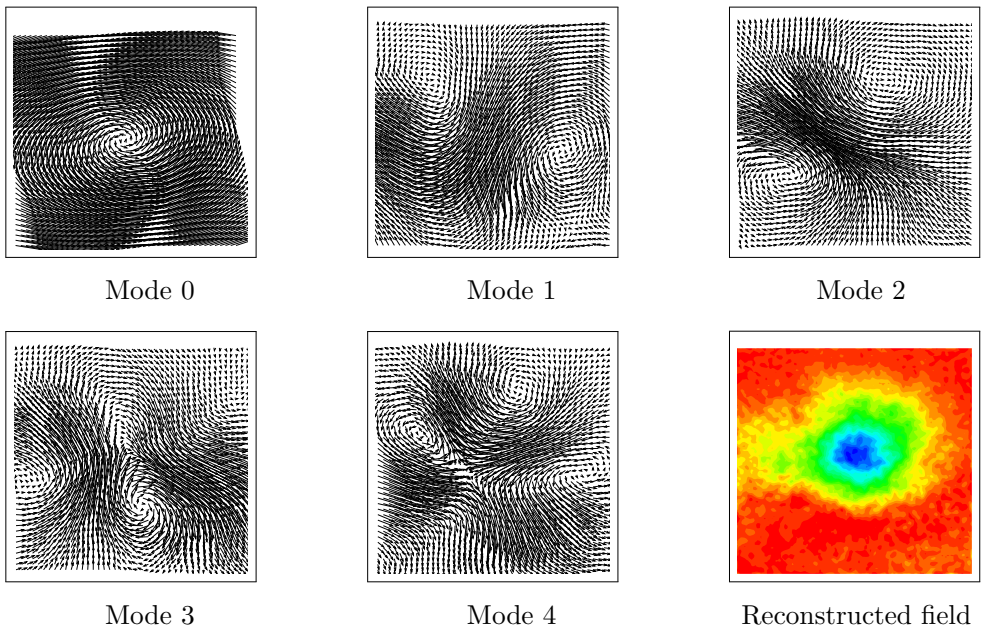

Figure 6. The mean and the first four mode shapes from the POD of tip vortex $V_A = 240°$, followed by a reconstruction of the vorticity in the first snapshot with 7 modes.

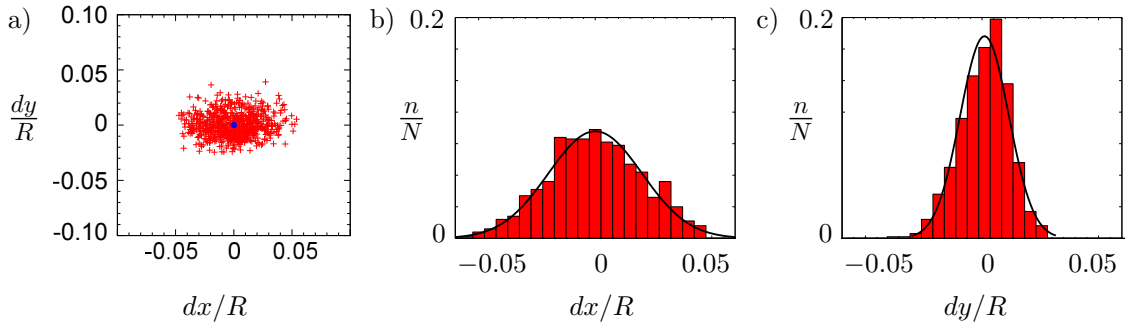

Figure 7. a) Scatter plot of the instantaneous vortex cores for tip vortex 2, relative to the mean core location, and binned histograms of the spread of the b) axial deviation and c) radial deviation of the cores. The curves are Gaussian probability density functions of each spread.

4. Conclusions

Planar PIV measurements of the wake behind a model turbine have been presented. The phase-locked results of the tip vortices reveal the mutual induction between the helical vortices, and their evolution suggesting a pairing downstream. Length scale filtering using POD and topology-based vortex identification post-processing removed small scales of turbulent fluctuations and inherent technique errors, which revealed an unsteady meander of the vortex cores at phase-locked positions up to the point of vortex pairing. The results show that this approach can capture the unsteady behaviour of the vortices and provide a means of investigating the characteristics of the vortex signature's meander. This approach could also be used to provide robust quantification of vortex properties and to investigate how the vortices pair downstream. Finally, it would be of interest to investigate the link between the vortex meander and the modes of the helical filament predicted by linear stability analysis.

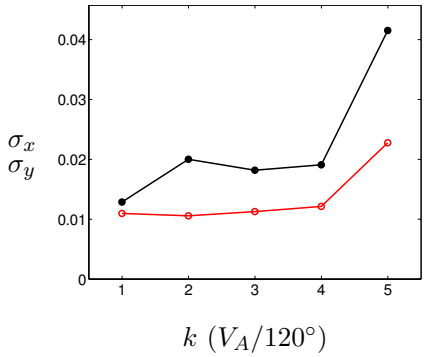

Figure 8. Axial (black filled circles)) and radial (red open circles) standard deviation of the first 5 tip vortices in the wake of the turbine.

5. Acknowledgements

This work was supported by the Australian Research Council through Discovery Project DP1096444.

6. References

[1] Okulov V L and Sørensen J N 2007 *J. Fluid Mech.* **576** 1–25
[2] Caradonna F 1999 *J. Am. Heli. Soc.* **44** 101–108
[3] Bhagwat M J and Leishman J G 2000 *J. Am. Heli. Soc.* **45** 165–178
[4] Felli M, Camussi R and Felice F D 2011 *J. Fluid Mech.* **682** 5–53
[5] Okulov V L 2004 *J. Fluid Mech.* **521** 319–342
[6] Widnall S 1972 *J. Fluid Mech.* **54** 641–663
[7] Wood D H and Boersma J 2001 *J. Fluid Mech.* **447** 149–171
[8] Larsen G C, Madsen H A, Bingl F, Mann J, Ott S, Srensen J N, Okulov V, Troldborg N, Nielsen M, Thomsen K, Larsen T J, and RMikkelsen 2007 Dynamic wake meandering modeling Tech. Rep. Report No. R-1607 Ris National Laboratory, Technical University of Denmark
[9] Vermeer L J, Sørensen J N and Crespo A 2003 *Prog. Aerosp. Sci.* **39** 467–510
[10] Sørensen J N 2011 *J. Fluid Mech.* **682** 1–4
[11] Barthelmie R J, Hansen K, Frandsen S T, Rathmann O, Schepers J G, Schlez W, Phillips J, Rados K, Zervos A, Politis E S and Chaviaropoulos P K 2009 *Wind Energy* **12** 431–444
[12] Gupta B P and Loewy R G 1974 *AIAA J.* **12** 1381–1387
[13] Hattori Y and Fukumoto Y 2009 *Phys. Fluids* **21** 014104
[14] Vermeer L J 2001 A review of wind turbine wake research at tudelft *A Collection of the 2001 ASME Wind Energy Symposium Technical Papers* (New York: ASME) pp 103–113
[15] Walther J H, Guénot M, Machefaux E, Rasmussen J T, Chatelain P, Okulov V L, Sørensen J N, Bergdorf M and Koumoutsakos P 2007 *J. Phys.: Conf. Ser.* **75** 012034
[16] Alfredsson P A and Dahlberg J A 1979 A preliminary wind tunnel study of windmill wake dispersion in various flow conditions Tech. rep. The Aeronautical Research Institute of Sweden aU-1499, part 7
[17] Ivanell S, Mikkelsen R, Sørensen J N and Henningson D 2010 *Wind Energy* **13** 705–715
[18] Schepers J and HSnel 2007 Model experiments in controlled conditions, final report Tech. Rep. ECN-E–07-042 The energy research center of the Netherlands
[19] Sherry M, Sheridan J and Lo Jacono D 2013 *Exp. Fluids* **54** 1–19
[20] Glauert H 1935 *Airplane propellers, Aerodynamic theory edited by W. F. Durand* (New York: Dover) pp 169–360
[21] Shen W Z, Mikkelsen R M, Sørensen J N and Bak C 2005 *Wind Energy* **8** 457–475
[22] Fouras A, Lo Jacono D and Hourigan K 2008 *Exp. Fluids* **44** 317–329
[23] Berkooz G, Holmes P and Lumley J L 1993 *Annu. Rev. Fluid Mech.* **25** 539–575
[24] Sirovich L 1987 *Q. Appl. Math.* **45** 561–571
[25] Graftieaux L, Michard M and Grosjean N 2001 *Meas. Sci. Tech.* **12** 1422–1429
[26] Raffel M, Willert C and Kompenhans J 2002 *Particle image velocimetry: a practical guide* (New York: Springer)
[27] Chakraborty P, Balachandar S and Adrian R J 2005 *J. Fluid Mech.* **535** 189–214

[28] Epps B P and Techet A H 2010 *Exp. Fluids* **48** 355–367